

On-ground calibration of the X-ray, gamma-ray, and relativistic electron detector onboard TARANIS

Yuuki Wada^{a,*} Philippe Laurent^{b,c} Damien Pailot^c Ion Cojocari^b
Eric Bréelle^c Stéphane Colonges^{d,c} Jean-Pierre Baronick^c François Lebrun^{b,c}
Pierre-Louis Blelly^d David Sarria^e Kazuhiro Nakazawa^{d,f}
and Miles Lindsey-Clark^c

^aOsaka University, Graduate School of Engineering, Division of Electrical, Electronic,
and Infocommunications Engineering, Osaka, Japan

^bService d'Astrophysique, IRFU/DRF, CEA Saclay, Gif-sur-Yvette, France

^cUniversité de Paris/CNRS, Laboratoire Astroparticule et Cosmologie, Paris, France

^dInstitut de Recherche d'Astrophysique et Planétologie, Toulouse, France

^eUniversity of Bergen, Birkeland Centre for Space Science, Bergen, Norway

^fNagoya University, Kobayashi-Maskawa Institute for the Origin of Particles and the Universe,
Nagoya, Japan

ABSTRACT. We developed the X-ray, gamma-ray, and relativistic electron detector (XGRE) onboard the Tool for the Analysis of RAdiation from lightNings and Sprites (TARANIS) satellite, to investigate high-energy phenomena associated with lightning discharges such as terrestrial gamma-ray flashes and terrestrial electron beams. XGRE consisted of three sensors. Each sensor has one layer of LaBr₃ crystals for X-ray/gamma-ray detections and two layers of plastic scintillators for electron and charged-particle discrimination. Since 2018, the flight model of XGRE was developed, and validation and calibration tests, such as a thermal cycle test and a calibration test with the sensors onboard the satellite, were performed before the launch of TARANIS on 17 November 2020. The energy range of the LaBr₃ crystals sensitive to X-rays and gamma rays was determined to be 0.04 to 11.6 MeV, 0.08 to 11.0 MeV, and 0.08 to 11.3 MeV for XGRE1, 2, and 3, respectively. The energy resolution at 0.662 MeV (full width at half maximum) was 20.5%, 25.9%, and 28.6%, respectively. The results from the calibration test were then used to validate a simulation model of XGRE and TARANIS. By performing Monte Carlo simulations with the verified model, we calculated effective areas of XGRE to X-rays, gamma rays, electrons, and detector responses to incident photons and electrons coming from various elevation and azimuth angles.

© 2024 Society of Photo-Optical Instrumentation Engineers (SPIE) [DOI: [10.1117/1.JATIS.10.2.026005](https://doi.org/10.1117/1.JATIS.10.2.026005)]

Keywords: TARANIS; x-ray, gamma-ray, and relativistic electron detector; terrestrial gamma-ray flash; terrestrial electron beam; high-energy atmospheric physics

Paper 23143G received Dec. 3, 2023; revised Apr. 9, 2024; accepted Apr. 16, 2024; published May 7, 2024.

1 Introduction

While lightning discharges are well-known atmospheric phenomena, recent studies have revealed that they are also associated with transient luminous events (TLEs¹) and high-energy phenomena.² Terrestrial gamma-ray flashes (TGFs) are high-energy atmospheric phenomena coincident with lightning discharges.^{3,4} They have typical durations ranging from tens to

*Address all correspondence to Yuuki Wada, wada@yuuki-wd.space

hundreds of microseconds,⁵ and the energy of gamma rays extends up to >20 MeV.⁴ Since the discovery³ made by the Burst and Transient Source Experiment (BATSE) onboard the Compton Gamma-Ray Observatory (CGRO), TGFs have been detected by in-orbit satellites such as the Reuven Ramaty High-Energy Solar Spectroscopic Imager⁴ (RHESSI), the Gamma-ray Burst Monitor (GBM) of Fermi,^{6,7} Astro-Rivelatore Gamma an Immagini Leggero^{8,9} (AGILE), BeppoSAX,¹⁰ and the Atmospheric-Space Interaction Monitor^{11,12} (ASIM) onboard the International Space Station.

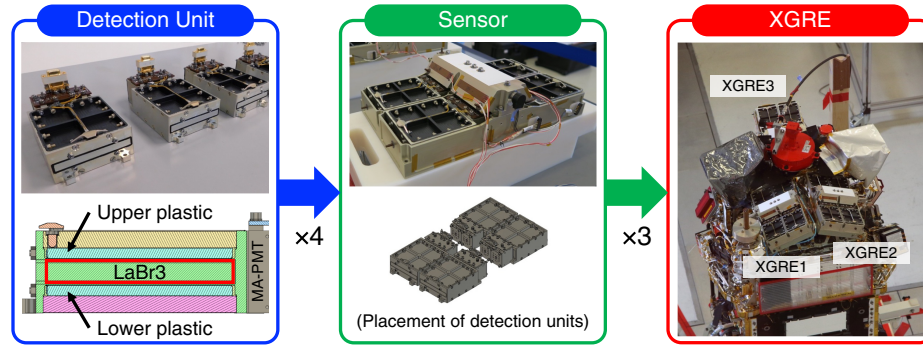
TGFs are thought to be bremsstrahlung photons from relativistic electrons, accelerated by strong electric fields in lightning. The relativistic runaway electron avalanche¹³ (RREA) is a promising theory for electron acceleration and multiplication by electric fields in the dense atmosphere. On the other hand, gamma-ray fluxes measured by satellite observations cannot be explained by electron-multiplication factors achieved by the RREA process.¹⁴ While more efficient electron-multiplication mechanisms such as the cold-breakdown^{15,16} and the relativistic feedback models^{17,18} have been proposed, definitive solutions have not been reached yet.

Among TGF candidates detected by BATSE/CGRO, RHESSI, AGILE, Fermi-GBM, and ASIM, some events have a duration longer than 1 ms. They are now interpreted as terrestrial electron beams (TEBs), rather than TGFs.^{19–21} Gamma-ray photons of a TGF can create electrons by Compton scatterings and pair productions and positrons by pair productions in the atmosphere. The produced electrons and positrons sometimes reach the satellites and are detected as a TEB. The electrons and positrons can be trapped by and move along a magnetic-force line of the Earth. Since electrons travel various distances along the magnetic fields, the duration of TEBs is typically longer than that of TGFs. In some cases, TEBs can be detected far from the parent lightning discharges. TEBs with enough positrons make a significant peak of the annihilation line at 511 keV in their energy spectrum.²⁰

One of the powerful tools to reveal the source mechanism of TGFs is multi-wavelength observations. Radio-frequency measurements are useful to observe parent lightning discharges of TGFs and have revealed that TGFs were produced during leader progression²² and/or coincident with distinct classes of low-frequency pulses called energetic in-cloud pulses^{23,24} and slow pulses.²⁵ Also, ASIM has optical cameras/photometers and X-ray/gamma-ray detectors, and investigates the relation between TGFs and lightning flashes²⁶ and between TGFs and TLEs.^{11,27}

The Tool for the Analysis of RAdiation from lightNIngs and Sprites (TARANIS) was a satellite mission developed by the National Centre for Space Studies of France (CNES), to investigate the relationship between lightning discharges and TLEs, TGFs, and TEBs.²⁸ TARANIS was a 200-kg satellite with the Myriade platform of the CNES, and consisted of six instruments: MicroCameras and Photometers; X-ray, gamma ray, and relativistic electron detector (XGRE); Instrument Détecteurs d’Electrons Energétiques (energetic electron detector); Instrument de Mesure du champ Electrique-Basse Fréquence (an instrument for low-frequency measurements); Instrument de Mesure du champ Electrique-Haute Fréquence (an instrument for high-frequency measurements); and Instrument de Mesure du champ Magnétique (an instrument for magnetic wave measurements), with the Multi Experiment Interface Controller equipment (MEXIC). The satellite was developed in collaboration with the Laboratory of Physics and Chemistry for Environment and Space, Alternative Energies and Atomic Energy Commission, Research Institute in Astrophysics and Planetology, Laboratory for Atmospheres and Space Observations, Laboratory Astroparticles and Cosmology (APC), Stanford University in the US, Institute of Atmospheric Physics and Charles University in the Czech Republic, and Space Research Centre of Polish Academy of Sciences.

At 22:52 on November 17, 2020, in Universal Coordinated Time (UTC), TARANIS was launched by the VEGA17 rocket of Ariane Space from the Kourou Space Center in French Guiana. TARANIS was planned to be transported into a sun-synchronous orbit at a 700-km altitude. However, the launch failed due to a malfunction at the fourth stage of the launcher, and unfortunately, the mission was lost. While the scientific mission that TARANIS was aiming at cannot be achieved, the development process of TARANIS is of great importance for future space missions. In the present paper, we report the on-ground validation and calibration campaign of the XGRE and its performance verification with Monte Carlo simulations. Throughout the paper, the time is described in UTC.

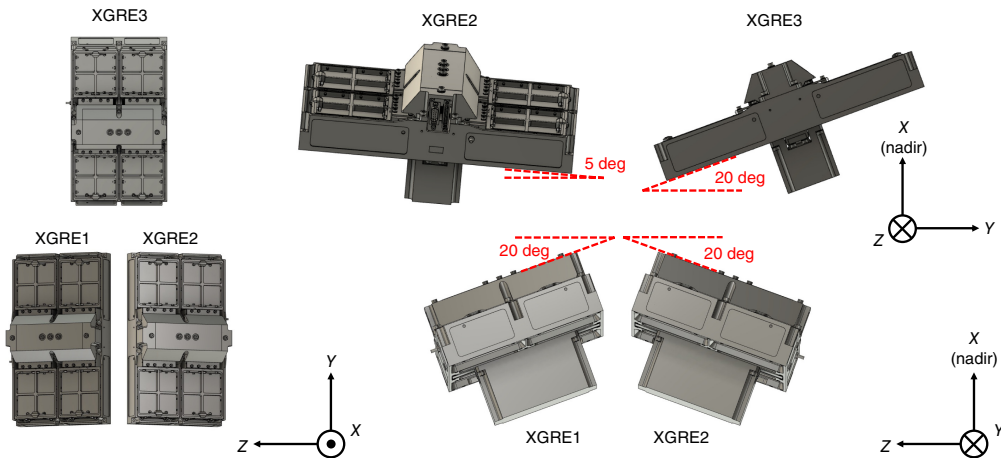
**Fig. 1** Composition of the XGRE.

2 XGRE

XGRE was the core detector on TARANIS for studying high-energy phenomena in lightning. It was designed to be sensitive to X-rays, gamma rays, and relativistic electrons to detect mainly TGFs and TEBs, which are mainly caused by lightning discharges. It was also sensitive not only to high-energy radiation from lightning discharges but also to one from space such as gamma-ray bursts (GRBs). The mission-required performance was to have sensitivity to X-rays and gamma rays of 0.02 to 10 MeV and electrons of 1 to 10 MeV. Since X-rays below 100 keV are susceptible to attenuation in the atmosphere, their energy spectra can be used to estimate the generation height of TGFs. The XGRE was mainly developed by APC/Paris.

XGRE consisted of three sensors. Figure 1 shows the configuration and composition of XGRE, and the three sensors mounted on the satellite. The sensors were mounted in the nadir direction of the satellite (Earthside) and were most sensitive to X-rays, gamma rays, and electrons emitted directly upward from the Earth. Each sensor was identical, but the angle at which it was mounted was different. Figure 2 shows the mounting angle of the sensors. XGRE1 and XGRE2 were tilted 20 deg around the Y axis and 5 deg around the Z axis. XGRE3 was tilted 20 deg around the Z axis. Since the effective area of XGRE changes with respect to the incoming direction of X-rays and gamma rays due to the difference in the mounting angle of each sensor, the difference in count rates of the sensors can be used to estimate the source location of TGFs.

Each sensor consisted of four detection units. Each detection unit contained an $84 \times 90 \times 8.7 \text{ mm}^3$ LaBr₃ scintillation crystal (manufactured by Saint-Gobain). Due to its hygroscopic nature, the LaBr₃ crystal was housed in aluminum with a thickness of 2 mm. Two $84 \times 90 \times 5 \text{ mm}^3$ plastic scintillators (BC400 by Saint-Gobain) were arranged to sandwich the LaBr₃ crystal. Figure 1 shows the appearance and cross-section of detection units. The nadir side was the upper plastic, and the space side was the lower plastic scintillator. Particle discrimination can be performed by taking coincidence counting of the LaBr₃ crystal and the plastic scintillators;

**Fig. 2** Mounting geometry of the XGRE.

X-rays or gamma rays when each crystal is hit alone; electrons within the measurable energy range when the LaBr₃ and one plastic scintillators are hit simultaneously; and high-energy electrons, positrons, and other charged particles exceeding the measurable energy range when three crystals are hit simultaneously.

Scintillation photons from each scintillator were read out from the side with two Hamamatsu multi-anode photomultipliers (MA-PMTs) R8900. R8900 is a 16-pixel MA-PMT, with four channels in the upper row for reading out the upper plastic scintillator, eight channels in the middle two rows for LaBr₃, and the lower row for reading out the lower plastic scintillator. Each XGRE sensor has two electronic boards, the analog front-end (FEA) and the digital front-end (FEN). The FEA has three separate analog chains corresponding to the upper/lower plastics and the LaBr₃ scintillator readout. The signals coming from the four detection units forming one sensor are connected together; thus, the dead-time percentage is dictated by the particle flux incident on the sensor. A stand-alone charge preamplifier A250F (Amptek) and a CR-RC shaper form each analog chain. The preamplifier is equipped with an active reset, which sets a fixed deadtime of 350 ns, and the gain is tailored to the light output of the different scintillators. On the FEN, dedicated radiation-hard ADCs are used, with a 14-bit resolution for the LaBr₃ read-out and 12 bits for the plastics. The read-out sequence is controlled by an FPGA that manages the preamplifier reset, the ADC operation, and the communication with the dedicated XGRE analyzer (XGA) in MEXIC. The final data packets are generated by XGA. XGA extracted and registered the peak value, detection time, sensor type, and scintillator type for pulse signals above a threshold. During normal operation, only the energy spectrum and light curves of each sensor and each scintillator were saved at regular intervals. Once XGA detected a sudden increase in count rate due to high-energy phenomena such as TGFs, TEBs, or GRBs, the peak value, detection time, sensor type, and scintillator type were saved and sent to the onboard computer of the satellite. Besides, one sensor had two high voltage (HV) modules. One HV module supplies HV to two detection units, i.e., four MA-PMTs.

3 On-Ground Validation and Calibration

The on-ground validation and calibration tests were performed in three steps: with the detection units, with the sensors, and with the satellite. A total of 16 flight models of the detection units were produced, and validation tests were conducted at APC in February 2018. In the test, we measured the variation in gain due to the characteristics of MA-PMTs, the analog circuit, and the optical bonding. Then, we selected 12 of the 16 units with better performance as flight models and 4 units as spare models.

After the sensors were validated at APC, a thermal-cycle test using the flight models was conducted from April to May 2018, and then, a thermal-vacuum test using the spare sensor was conducted from June to July 2018. These tests were performed at the Laboratory of Space Studies and Instrumentation in Astrophysics (LESIA) of the Paris Observatory. In normal cases of satellite development, a thermal-vacuum test is performed with a flight model to validate functions in the space environment. On the other hand, we did not perform the thermal-vacuum test on the flight models as the LaBr₃ crystals used in the detection units are highly hygroscopic inorganic crystals, and hence, an aluminum housing is indispensable to prevent this. However, we discovered that the vacuum test may reduce the air tightness of the housing, and humid air may enter after the vacuum test, degrading the detector's performance (of course, even if the housing tightness is reduced in space, this cannot occur due to the absence of air). Therefore, the flight models were subjected only to a thermal cycle test in a chamber filled with dry nitrogen gas. As an alternative, a thermal-vacuum test was performed on the spare sensor test, which revealed to be finally successful.

In November 2018, the validation tests of XGRE alone were completed, and the XGRE was handed over from APC to CNES in Toulouse. After the XGRE installation on the satellite (March to April 2019) and vibration and acoustic tests on the entire satellite (June 2019), a calibration test of XGRE with the entire satellite was performed using radiation sources. Although the launch was delayed due to the COVID-19 lockdown and the failure of VEGA15, the satellite was transported from Toulouse to the Guiana Space Center in September 2020.

A thermal vacuum test of the entire satellite was conducted from January to February 2019, but the XGRE flight model was not mounted on the satellite at that time; instead, a dummy load was mounted. In the present paper, we report in detail the temporal resolution verification, the thermal-cycle test for the flight-model sensors, and the calibration test with the sensors onboard the satellite.

3.1 Verification of Temporal Resolution with Detection Units

TGFs are a phenomenon in which photons arrive almost instantaneously (from tens to hundreds of microseconds). It causes pile-ups, which are superpositions of photon pulses. When a pile-up occurs, the measurement of the number and energy of photons becomes inaccurate, and it should be avoided as much as possible. Therefore, by dividing one sensor into four detection units, XGRE is designed to reduce the number of photons per detection unit and reduce pile-ups. We verified the photon measurement ability of the detection unit alone in a high count-rate environment.

A single detection unit was used as the experimental setup. A scintillator was not attached to the PMT, and pulsed light using an LED was used instead of scintillation light. Of the pixels of the MA-PMT, the upper and lower rows that read out the plastic scintillators were masked, and the LED light was set to be irradiated on the two middle rows that read out LaBr₃. LED pulses were emitted for exactly 1 s at frequencies of 1 kHz, 10 kHz, 100 kHz, 300 kHz, 500 kHz, 1 MHz, 1.5 MHz, and 2 MHz. The pulses are not generated at random intervals but at regular intervals. Three types of LED brightness were tested, corresponding to 670 keV, 5.0 MeV, and 9.7 MeV equivalent. The duration of LED pulses was 75 ns, enough short compared with the shaping time of the preamplifier and considered as a delta function.

Regardless of the brightness of the LED, it is confirmed to record pulses up to 1 MHz without missing any pulses. Also, when using LED pulses equivalent to 670 keV and 5.0 MeV, it was possible to obtain pulses up to 1.5 MHz (testing at 1.5 MHz at 9.7 MeV may cause overcurrent in the high-voltage module so not tested). In the case of LED pulses equivalent to 670 keV, measurements were also performed at 2 MHz, but pile-up occurred and only ~80% of the pulses could be counted. Therefore, the pulse measurement capability was demonstrated up to 1.5 MHz.

Excessive current may flow between the dynodes of a photomultiplier at high count rates, which can cause a drop in HV due to the current limits of the high-voltage supply module. It causes gain variation, which may affect the observation results. In addition, large current discharges capacitors in PMT dividers excessively, which also causes significant gain changes. Therefore, by changing the brightness and frequency of the LED pulses with the same setup above, we investigated the gain variation, namely, the variation in the peak value of the amplifier outputs.

The results are shown in Fig. 3. With all the brightnesses of LED, a decrease in gain was observed at count rates of 1 MHz or higher. In the case of 0.67-MeV equivalent, no gain

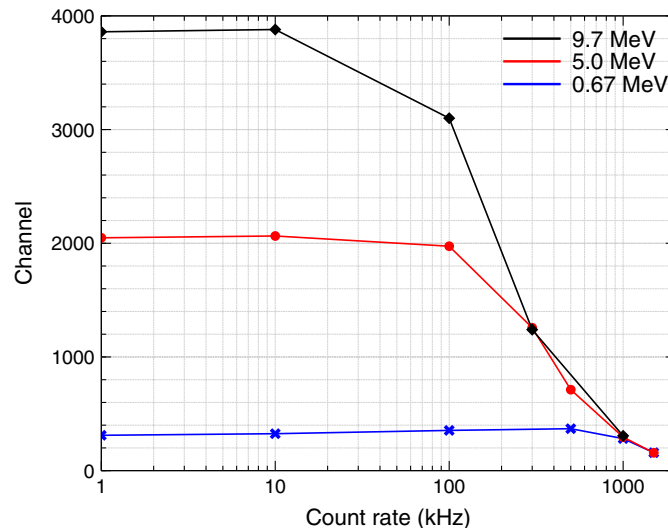


Fig. 3 Relation between pulse frequency and peak height.

fluctuation was observed up to 500 kHz, but the gain decreased slightly at 1 MHz. With 5.0-MeV equivalent pulses, the gain was constant up to 100 kHz, but a decrease was seen above 300 kHz. This is more noticeable in the case of 9.7 MeV, where the gain was constant up to 10 kHz, but decreases above 100 kHz. Note that this situation assumes a uniform train of pulses. On the other hand, the arrival time of photons from TGFs is usually random, and the maximum count rate in actual observation situations could be degraded (by approximately one-third to half).

3.2 Thermal Cycle Test of Sensors

The thermal-cycle test was conducted to verify the operation of XGRE in thermal conditions of the space environment and to investigate the characteristics of gain variation due to temperature changes. The test was performed with a thermal-cycle chamber EXCAL 2221-T/H at LESIA. As shown in Fig. 4(a), three sensors were placed inside the chamber using a supporting structure dedicated to this test. The maximum and minimum temperature during the test was 35°C and -25°C, respectively. The maximum temperature transition rate was 8°C per hour. This slew rate is determined by the specification of the chamber, also within the requirement of the LaBr₃ producer (<20°C per hour). A total of four cycles were performed in the test.

The test started at 09:40 UTC on April 25, 2018, and ended at 16:40 UTC on May 10, 2018, with the first cycle from 11:46 on April 25 to 23:32 on April 27, second cycle from 23:22 on May 1 to 18:40 on May 2, third cycle from 7:15 on May 3 to 20:47 on May 4, and fourth cycle from 22:53 on May 8 to 18:17 on May 9. To prevent dew condensation and performance deterioration of the LaBr₃ crystals, the chamber was filled with 99.995%-purity dry nitrogen gas. As shown in Fig. 4(b), an ⁸⁸Y radiation source was used during the test and irradiated the three sensors from the side of the chamber. Energy spectra of each sensor were acquired approximately every 30 min, and the gain variation was analyzed by tracing the center of the 898-keV absorption peak of ⁸⁸Y in the LaBr₃ crystals. The temperature was measured by a platinum resistance temperature sensor PT-100 (Lake Shore Cryotronics Inc.) attached to each sensor.

Figure 5 shows the temperature and gain variation of each sensor during the thermal-cycle test. The gain variation was tracked by fitting the total absorption peak of ⁸⁸Y at 898 keV with a Gaussian function for the energy spectra acquired every 30 min. Figure 6 shows the correlation between temperature and gain. In the cycle on the high-temperature side, a negative correlation was observed, in which the gain decreased as the temperature increased. In the second cycle, when the operation was stable, the gain variation was 31%, 34%, and 35% for XGRE1, 2, and 3, respectively, for the temperature change from 20°C to 35°C. They correspond to the variation rate of 2.1% K⁻¹, 2.3% K⁻¹, and 2.3% K⁻¹, respectively. On the other hand, in the cycle on the low-temperature side, the relationship between gain and temperature was not a monotonic function and not a one-to-one correspondence. For XGRE1 and XGRE2, hysteresis was also observed in which the gain variation was different when the temperature was falling and when the

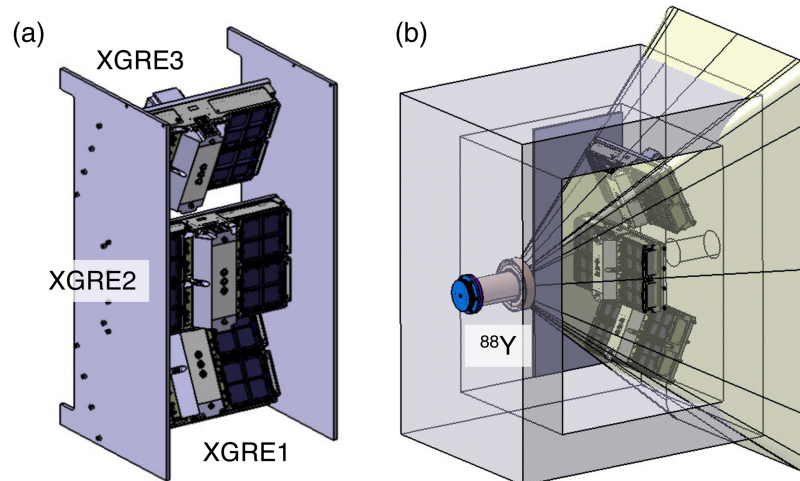


Fig. 4 Placement of three sensors during the thermal cycle test. (a) The sensors with a dedicated mounting jig. (b) Geometry of the radiation source.

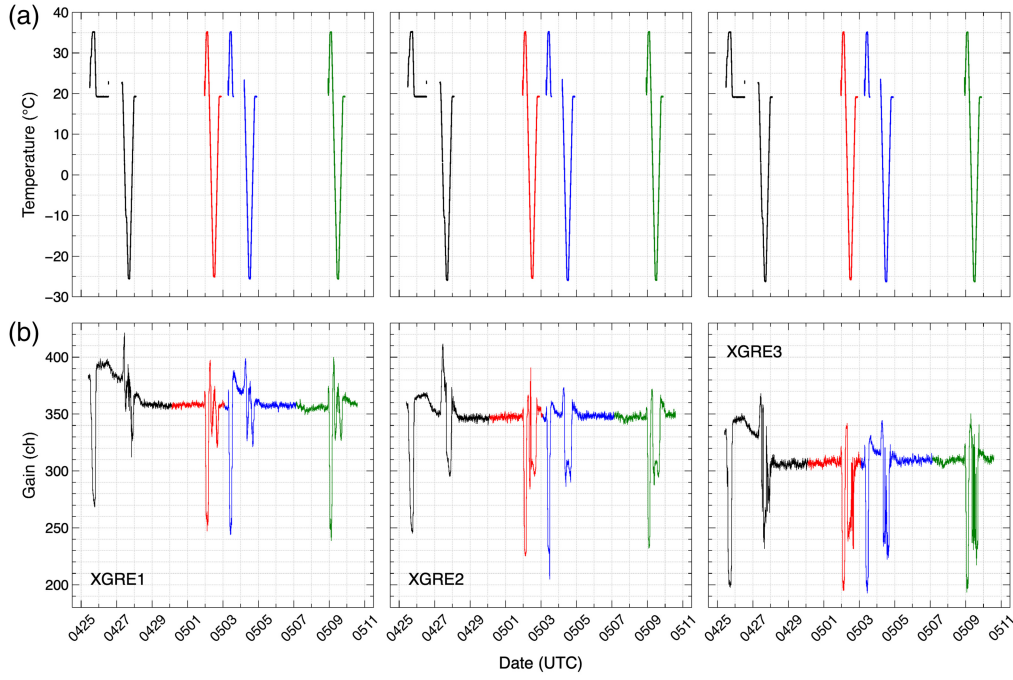


Fig. 5 Temperature (a) and gain (b) variation during the thermal-cycle test. Black, red, blue, and green lines indicate the first, second, third, and fourth cycles, respectively. The temperature profile was obtained only during the cycle operations, not during the temperature plateaux. The gain is the peak channel of the 898-keV line from ^{88}Y .

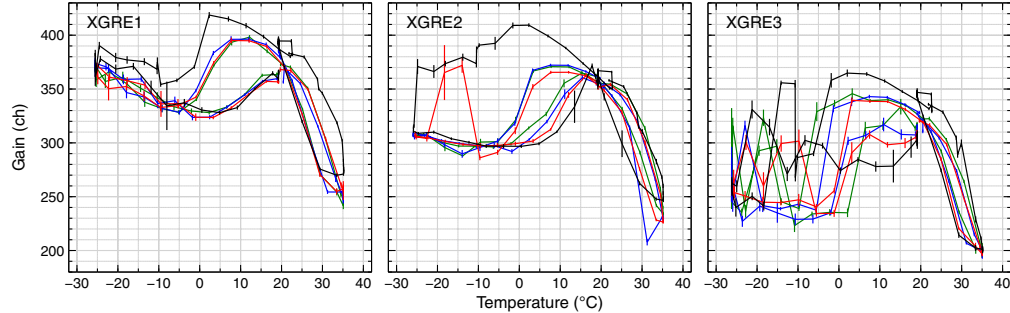


Fig. 6 Correlation between the temperature and gain profiles during the thermal-cycle test. Black, red, blue, and green lines indicate the first, second, third, and fourth cycles, respectively.

temperature was rising. Due to the difference in plateau temperature (not shown in Fig. 5), the gain of the first cycle during the temperature plateau is different from those of the other cycles.

Figure 7 shows examples of the energy spectra obtained with XGRE1 on the low-temperature side of the first cycle. At room temperature at 06:25UTC, we detect the 898-keV line of ^{88}Y around 380 ch, its Compton edge around 270 ch, the 1.84-MeV line of ^{88}Y around 770 ch, and its Compton edge around 630 ch. On the other hand, at 11:20 UTC, when the temperature was falling, the 898-keV emission line was separated into two peaks. At 14:36 UTC, when the temperature was falling further, the two peaks overlapped again to form a broadened emission line with a flat top. As described in Sec. 2, one sensor consisted of four detection units and two HV units, and one high-voltage unit served two detection units. The main factor of the gain variation is considered high-voltage variation due to temperature change. The output of one sensor was the sum of the outputs of the four detection units. However, if the two HV units have different characteristics of temperature, detection units connected to different high-voltage units could exhibit different gain variations. Therefore, the gains of the four detection units were not uniform depending on the temperature, and two peaks were generated. The hysteresis of the gain-temperature relation could make hard to precisely correct the gain variation by temperature,

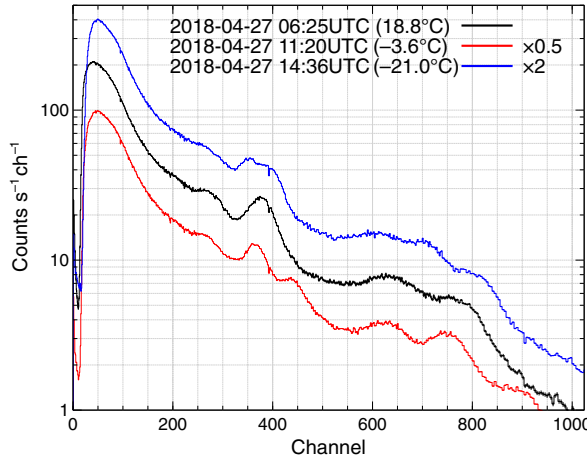


Fig. 7 Examples of energy spectra obtained by XGRE1 during the thermal-cycle test. The red and blue plots are shifted by a factor of 0.5 and 2, respectively, for visualization purposes.

and independent control of HV units or unifying the HV units will be required for a future design. In the analysis, when the 898-keV emission line was separated into two, each peak was fitted with Gaussian, and the average of the two emission line centers was taken as the gain.

3.3 Sensor Calibration Onboard Satellite

After the validation and calibration tests, XGRE was delivered to CNES and installed on the TARANIS satellite. The calibration test of XGRE attached to the satellite using radiation sources was performed from February to March 2020 at the CNES Toulouse Space Center. As shown in Fig. 8, the radiation sources irradiated the spacecraft from eight directions using a dedicated supporting structure. At position 1, gamma rays come to the detector vertically from the nadir direction (Earthside). At positions 2 to 4, the azimuth angles were set to 0, 240, and 120 deg, respectively, and the elevation angle was set to 43 deg. At positions 5 to 8, gamma rays come from the opposite side of the nadir (the space side). The elevation and azimuth angles are the same as positions 1 to 4. We utilized ^{137}Cs , ^{88}Y , ^{57}Co , and ^{241}Am sources. Their radioactivity at the time of calibration was 3.8, 3.2, 3.4, and 1.7 MBq, respectively. Each radiation source was enclosed in a collimator made of 95% tungsten and 5% iron–nickel and attached to the supporting structure. The aperture angle of the collimator was 52 deg. We performed a total of 32 measurements with 4 sources at 8 locations and one background measurement. The duration of each measurement is summarized in Table 1. Since gamma rays of ^{241}Am were out of the energy range of XGRE2 and 3, their analysis is only included for XGRE1.

Figure 9 shows the energy spectra measured by the LaBr₃ crystals when the radiation sources were placed at position 1. The background was subtracted for measurements with sources. In the measurements with ^{241}Am , ^{137}Cs , and ^{88}Y , the 60, 662, and 898 keV emission lines are detected, respectively. With the ^{57}Co source, a peak due to the emission lines at 122 and 136 keV is also found. An energy calibration function was calculated by fitting these emission

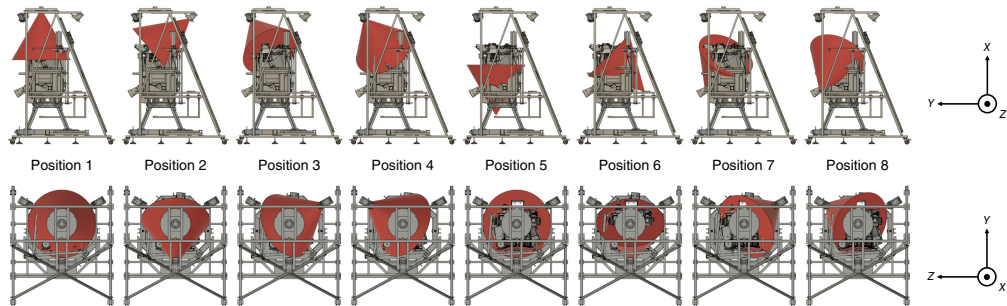


Fig. 8 Source positions for the calibration test with satellite. The red cones show irradiated regions.

Table 1 Duration of source measurements for the calibration test with satellite.

Source	Positions 1 to 4 (h)	Positions 5 to 8 (h)
^{137}Cs	0.40	0.33
^{88}Y	3.5	0.42
^{57}Co	0.26	1.0
^{241}Am	0.57	6.0
Background	6.6 hours	

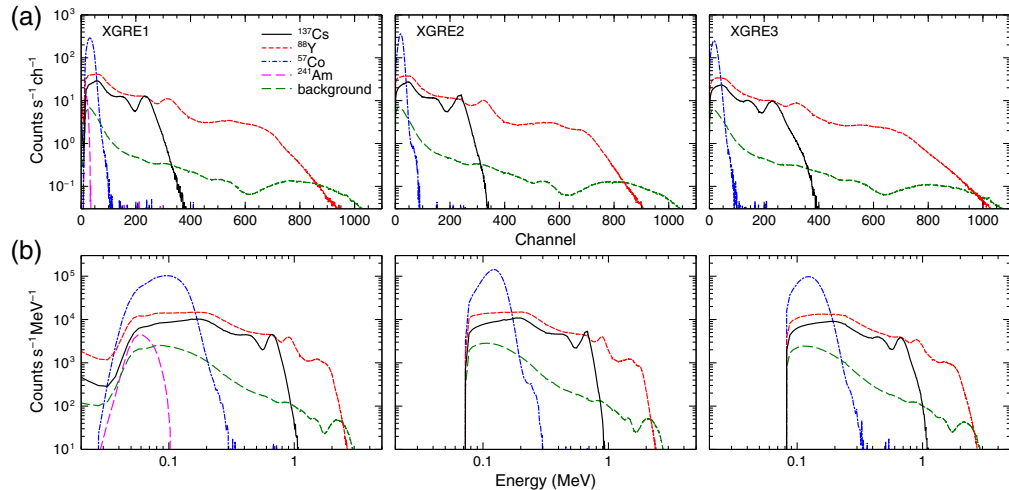


Fig. 9 Energy spectra obtained by LaBr_3 crystals during the calibration test with satellite. Radiation sources were at position 1. The spectra with the radiation sources are background-subtracted. (a) Raw spectra. (b) Calibrated spectra.

lines with a Gaussian function. Since the two emission lines of ^{57}Co cannot be resolved with the energy resolution of this sensor and were seen as one line, the energy center was calculated as 124 keV from the branching ratio of the two lines. For XGRE1, lines from ^{241}Am , ^{137}Cs , and ^{88}Y are used for the calibration, and ^{57}Co is used for XGRE2 and 3 instead of ^{241}Am .

The calibration function was obtained as follows:

$$\text{XGRE1: } E = 0.0058 + 2.82 \times 10^{-3} \times \text{ch} [\text{MeV}], \quad (1)$$

$$\text{XGRE2: } E = 0.0729 + 2.52 \times 10^{-3} \times \text{ch} [\text{MeV}], \quad (2)$$

$$\text{XGRE3: } E = 0.0808 + 2.56 \times 10^{-3} \times \text{ch} [\text{MeV}]. \quad (3)$$

The energy range of each sensor was 0.04 to 11.6 MeV, 0.08 to 11.0 MeV, and 0.08 to 11.3 MeV for XGRE1–3, respectively. XGRE1 registers energies below 0.04 MeV, but there seemed to be a cutoff below 0.04 MeV, and hence, above 0.04 MeV was reliable. In addition, the energy resolution [full width at half maximum (FWHM)] at 662 keV was 20.5%, 25.9%, and 28.5%, respectively.

Figure 10 shows the energy spectra of the LaBr_3 crystals with the ^{137}Cs source at each position. The intensity varies depending on the position of the radiation source. For example, in the measurements at positions 2 and 6, the intensities of XGRE1 and 2 were higher than that of XGRE3. These measurements are checked in Sec. 4 using Monte Carlo simulations.

Figure 11 shows the energy spectra obtained with plastic scintillators when the ^{137}Cs or ^{88}Y source was placed at position 1. Since plastic scintillators have small cross sections for photo-absorption, energy calibration is usually performed using a Compton edge. However, due to the

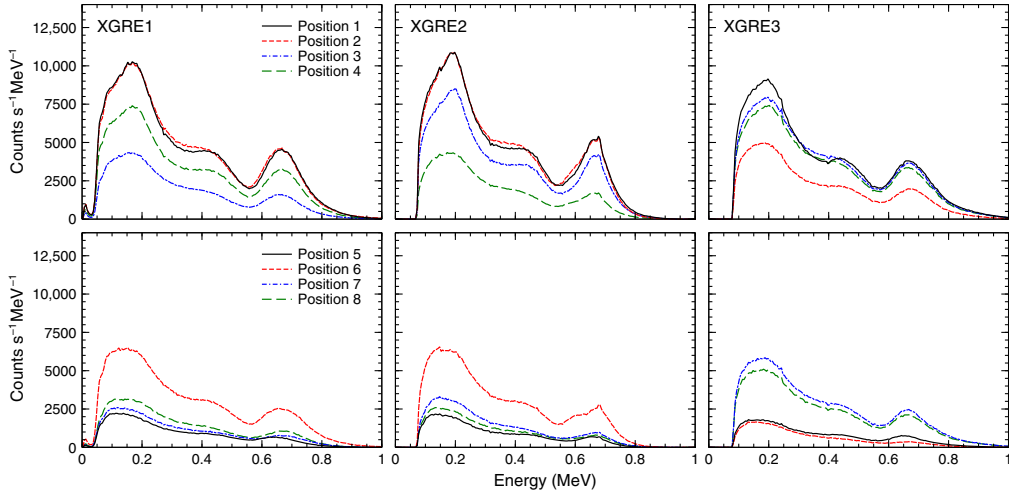


Fig. 10 Background-subtracted energy spectra obtained by LaBr₃ crystals during the calibration test with satellite, with the ¹³⁷Cs source at various positions.

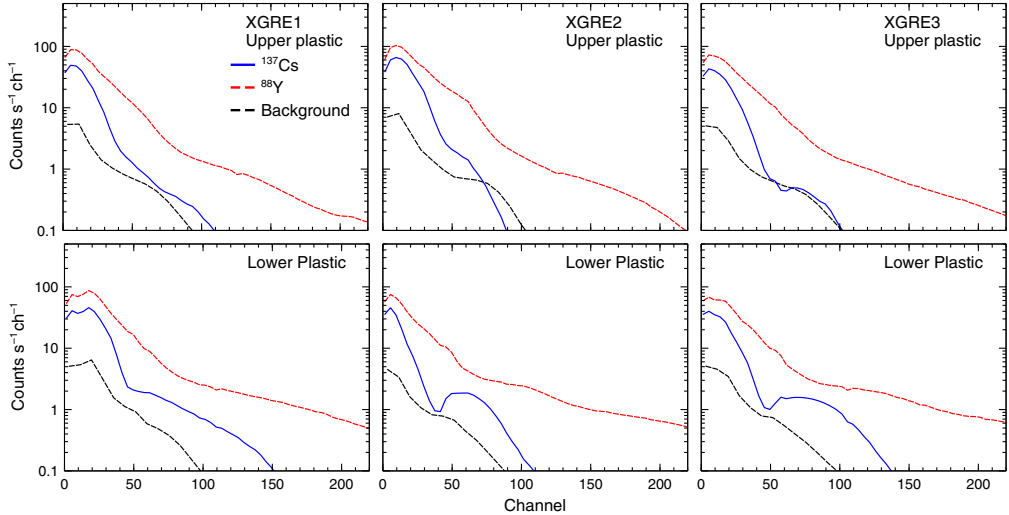


Fig. 11 Background-subtracted energy spectra obtained by plastic scintillators during the calibration test with satellite. The radiation sources were at position 1.

moderate energy resolution, the plastic scintillators of XGRE barely detect the Compton edge due to the 662-keV line of ¹³⁷Cs and the 898-keV line of ⁸⁸Y. Therefore, accurate energy calibration of the plastic scintillator was difficult with the gamma-ray sources, and a specific method had to be developed to calibrate the upper plastic scintillator (see Laurent et al.²⁹). Note that a valley-like structure in the energy spectra of lower plastic scintillators with ¹³⁷Cs is confirmed around channel 40, which seems not to be explained by general Compton-scattering features.

4 Performance Verification with Monte Carlo Simulations

In this section, we perform Monte Carlo simulations with a satellite model and validate the simulation results by comparing them with the measurement results obtained in the satellite calibration test. We also evaluate the characteristics of the XGRE, such as effective area, angular resolution, and electron detection, using the verified simulation model. Monte Carlo simulations were performed with Geant4 version 4.10.3^{30–32} and CADMsh version 1.1.³³ The satellite/detector models implemented in Geant4 are based on those used in Sarria et al.³⁴

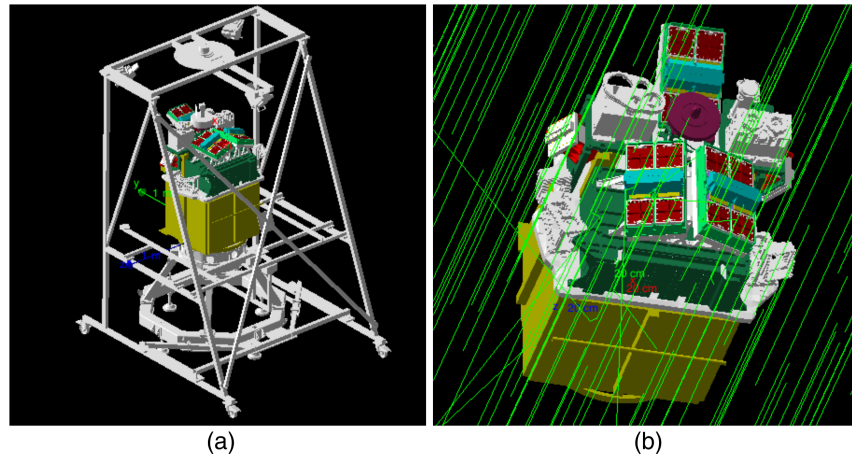


Fig. 12 Schematics of Geant4 simulations. (a) Simulation for the on-ground calibration test. (b) Simulation in the space environment.

4.1 Verification of Geant4 Model

We constructed a model simulating the calibration test with the satellite conducted at CNES and then performed Monte Carlo simulations. The simulation model is shown on the Fig. 12(a). The satellite/detector, a supporting structure for the satellite, a support for attaching the radiation sources, and a collimator for the radiation sources were implemented in the simulation space where the atmosphere was also implemented. Here, we generated gamma rays from the ^{137}Cs and ^{88}Y sources at positions 1 to 4, calculated the energy deposits in the LaBr_3 crystal of each sensor, and extracted the energy spectra. In the simulated spectrum, the energy resolution at FWHM on the calibration test was convoluted as follows:

$$\Delta E = \Delta E_{662} \times \left(\frac{E}{0.662 \text{ MeV}} \right)^{0.5}. \quad (4)$$

ΔE_{662} is the energy resolution at 0.662 MeV, which is 20.5%, 25.9%, and 28.5% for XGRE1–3, respectively.

Here, we assume that these energy resolutions are due to a reduced LaBr_3 optical efficiency, a consequence of the limited surface area of the optical contact between LaBr_3 crystals and PMTs (scintillation light losses), rather than electronic noises. The normalization of the simulation results was calculated from the number of gamma rays generated in the simulation, the radioactivity of the radiation sources during the calibration test, and the measurement time. In each simulation, 5×10^8 gamma rays were generated.

Figure 13 compares the simulated spectra with the spectra obtained in the calibration test. At any source type and source position, the emission line from the sources and their Compton scattering component is generally reproduced above 0.2 MeV by the simulation spectra. In the energy band below 0.2 MeV, the measurement results tend to exceed the simulation results, especially those with the ^{88}Y source. The low-energy component is highly susceptible to scattering by materials around the satellite and detector, and hence, it may cause the excess below 0.2 MeV (note that no floor nor walls were implemented in the simulation). Therefore, the simulation model is validated above 0.2 MeV and has an uncertainty of $\sim 15\%$ at a maximum below 0.2 MeV.

4.2 Effective Areas for X-Rays and Gamma Rays

Using the simulation model verified in Sec. 4.1, we calculated the effective area for X-rays and gamma-rays of XGRE. Here, the effective area is defined as an area for depositing at least the threshold energy in the detector. The simulation model is shown on Fig. 12(b). We prepared the satellite model in space orbit and generated photons in a vacuum. In the simulation, 10^9 photons from 0.02 to 10 MeV were emitted from a disk-shaped region with a radius of 1 m (a fluence of 3.18×10^4 photons cm^{-2}), and the effective area was calculated from the energy

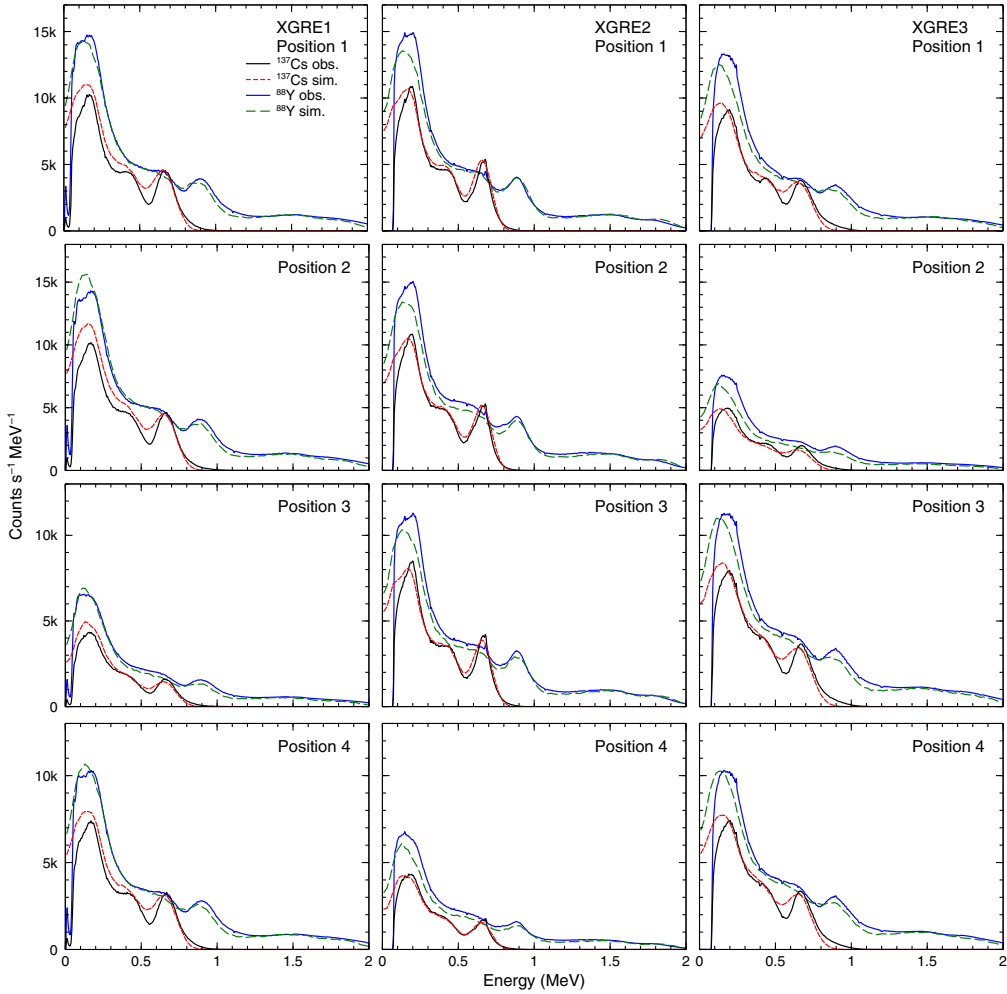


Fig. 13 Comparison of energy spectra obtained by the calibration test with satellite and by Monte Carlo simulations. Solid and dashed lines indicate measurement and simulation spectra, respectively.

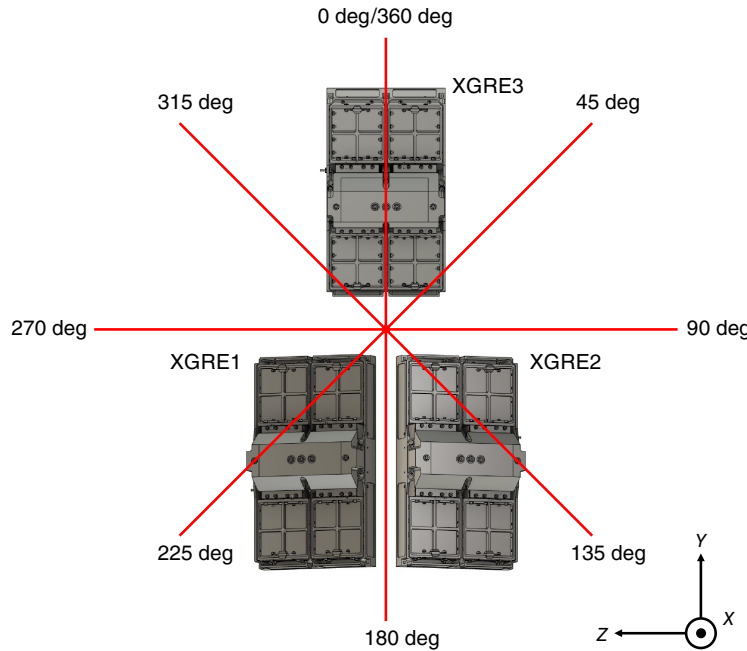
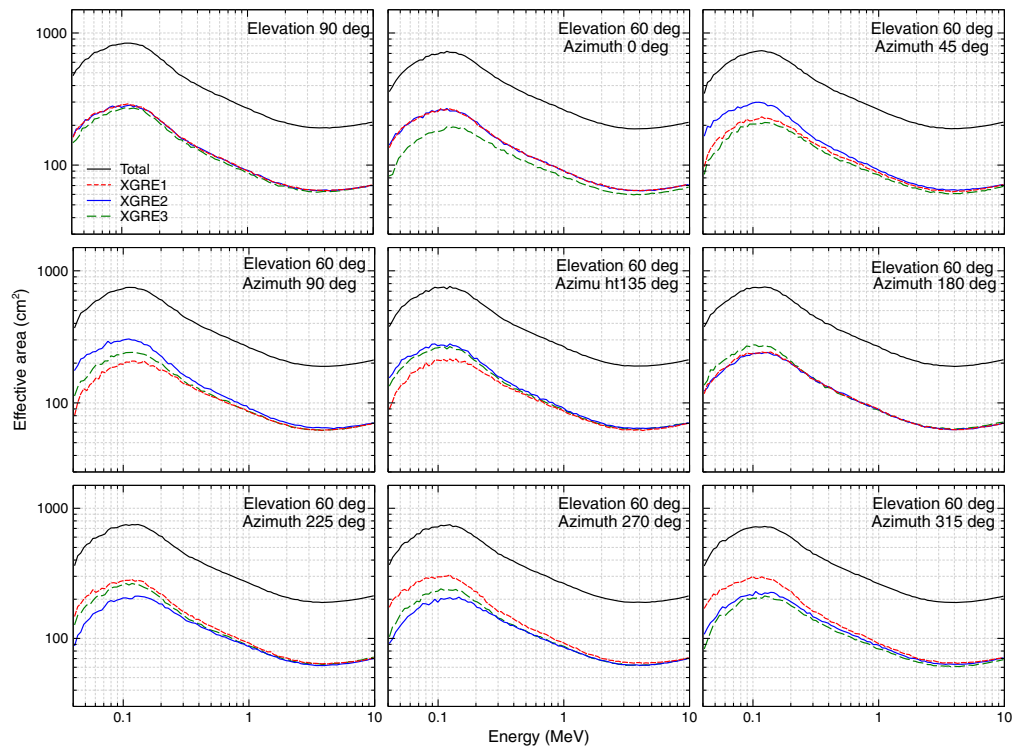
deposits in the LaBr₃ crystal. In addition, two elevation angles of 90 deg (the nadir direction) and 60 deg were set for the particle generation direction, and simulations were performed for eight azimuth angles when the elevation angle was 60°. The definition of azimuth angles is shown in Fig. 14.

Figure 15 shows the calculated effective area. At an elevation angle of 90 deg, the effective area reaches the maximum at 0.1 MeV, 838 cm² in total for the three sensors. Since the geometric area of the LaBr₃ scintillators at the elevation angle of 90 deg is 850 cm², the detection efficiency is 98.6% at 0.1 MeV. The effective area reaches the minimum at 3.5 MeV, 191 cm² in total for the three sensors. At this time, the detection efficiency is 22.8%. The result is consistent with the previous work.³⁴ In the band below 0.3 MeV at an elevation angle of 60 deg, the effective area of the sensors varies depending on the azimuth angle.

Then, we simulated an energy spectrum of a TGF detected by XGRE. Briggs et al.⁶ reported that a typical fluence of TGFs in an energy range of 0.2 to 40 MeV $F_{0.2-40 \text{ MeV}}$, detected by Fermi, was 0.7 photons cm⁻². Here, we assume a typical energy spectrum of TGFs² dN/dE

$$\frac{dN}{dE} \propto E^{-1} \exp\left(-\frac{E}{7.3 \text{ MeV}}\right), \quad (5)$$

where E is the energy of gamma rays. A fluence $F_{0.04-10 \text{ MeV}}$ in the observation range of XGRE1 0.04 to 10 MeV is then

**Fig. 14** Definition of azimuth angle.**Fig. 15** Effective areas of X-rays and gamma rays for various elevation and azimuth angles. The 90-deg-elevation angle means that photons come from the nadir direction. The definition of azimuth angle is in Fig. 14.

$$F_{0.04-10 \text{ MeV}} = F_{0.2-40 \text{ MeV}} \times \frac{\int_{0.04 \text{ MeV}}^{10 \text{ MeV}} E^{-1} \exp\left(-\frac{E}{7.3 \text{ MeV}}\right) dE}{\int_{0.2 \text{ MeV}}^{40 \text{ MeV}} E^{-1} \exp\left(-\frac{E}{7.3 \text{ MeV}}\right) dE} = 1.06 \text{ photons cm}^{-2}. \quad (6)$$

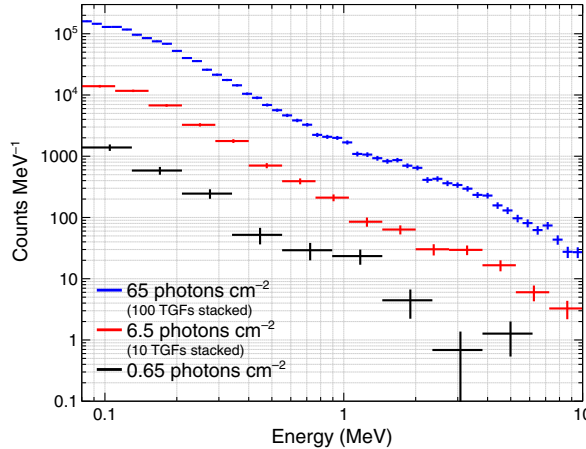


Fig. 16 Simulation spectra of TGFs by XGRE with various photon fluences. The fluence of $0.65 \text{ photons cm}^{-2}$ is an expected one of a typical TGF (see the main text).

This is a typical fluence at Fermi's orbital altitude of 550 km. Assuming that TGFs are typically produced at an altitude of 15 km, the fluence at the orbital altitude of TARANIS, 700 km, is

$$1.06 \times \left(\frac{550 - 15 \text{ km}}{700 - 15 \text{ km}} \right)^2 = 0.65 \text{ photons cm}^{-2}. \quad (7)$$

Figure 16 shows the simulated TGF spectrum assuming detection by XGRE. We performed simulations with the energy spectrum following Eq. (5), an elevation angle of 90 deg, and with three fluences of 0.65 , 6.5 , and $65 \text{ photons cm}^{-2}$ (1 TGF, 10 TGFs stacked, and 100 TGFs stacked, respectively). At the typical TGF fluence, $0.65 \text{ photons cm}^{-2}$, both the number of photons and the effective area of XGRE were small in the band above 5 MeV, and few photons were detected. Spectral analysis of a single TGF would be available only on the low-energy side. On the other hand, by performing a stacking analysis that adds spectra of multiple TGFs, it would be possible to discuss the power-law indexes and cut-off energies.

4.3 Effective Areas for Electrons

XGRE identified electrons coming from the nadir direction when the upper plastic and the LaBr_3 scintillators among the three ones in a detection unit detected energy deposits simultaneously; non-charged particles (mainly X-rays and gamma rays) when only one of the three scintillators was hit; electrons from space when the LaBr_3 and the bottom plastic scintillators were hit simultaneously; and high-energy charged particles such as protons and electrons with energies beyond the detection range when the three layers were hit simultaneously. When electrons are detected, their kinetic energy is deposited in the upper plastic and LaBr_3 scintillators, and the amounts of deposits depend on the energy of the incident electrons. Therefore, by generating electrons in a simulation and calculating the energy deposits in each scintillator, the incident energy of the electrons can be estimated from the energy deposits in the scintillators.

In the simulation, we used the same setup as in Sec. 4.2 (Fig. 12(b)), and generated 1 to 10-MeV electrons with a fluence of $3.18 \times 10^4 \text{ electrons cm}^{-2}$ (10^9 electrons in a 1 m radius disk) and an elevation angle of 90 deg. In a single particle run, electron detection was identified when the upper plastic and LaBr_3 scintillators detected energy deposits exceeding their energy threshold. For the LaBr_3 crystals, the energy threshold was 0.04 MeV for XGRE1 and 0.08 MeV for XGRE2 and 3 as determined by the satellite calibration. While the exact threshold for plastic scintillators has not been determined due to the difficulty of energy calibration, it was assumed to be 0.2 MeV. In real TEB cases, electrons are bound by Earth's magnetic field and have various pitch angles. Therefore, the represent simulation with parallel electron beams is limited, and further investigation is needed to apply this to realistic TEBs (beyond the scope of the present paper).

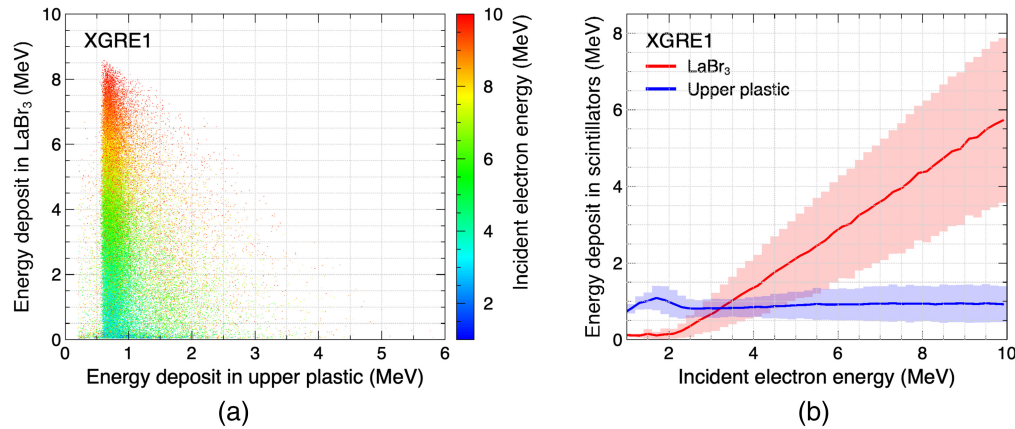


Fig. 17 Simulated behaviors of electrons in XGRE. (a) A scatter plot for the relation between energy deposits in LaBr₃ and upper plastic scintillators. The plot colors indicate initial electron energies. (b) Relations between incident electron energy and energy deposits in scintillators. The translucent areas show statistical error at one standard deviation.

Fig. 17(a) shows a scatter plot of the relationship between the energy deposit in the upper plastic and the LaBr₃ scintillator for electron detection by XGRE1. The color of the plot corresponds to the incident electron energy. The distribution of energy deposit in the plastic scintillators is concentrated around 0.6 to 1.2 MeV. On the other hand, energy deposits in LaBr₃ increase when incident electron energy increases. It is noted that the energy deposits in both the LaBr₃ and upper plastic scintillators show variations. Electrons continuously react with matter and deposit their kinetic energy through numerous scatterings called straggling. Since straggling is a stochastic process, the paths in the scintillator are slightly different even for electrons with the same incident energy, resulting in a difference in the energy deposit. To determine that the XGRE detected an electron, the electrons must penetrate the upper plastic scintillator and deposit all the rest kinetic energy in LaBr₃. Therefore, the energy deposit in the plastic scintillator is almost constant (determined by the thickness of the scintillator), and the remaining energy is deposited in LaBr₃.

Figure 17(b) shows the relation between incident electron energy and average energy deposits in each scintillator. In addition, the semi-transparent regions indicate the variation of energy deposits at one standard deviation. The average energy deposit in the plastic scintillators is around 1 MeV for the entire range of incident electron energy. Energy deposits in the upper plastic are at maximum with incident electron energies between 1.5 and 2 MeV. This is due to the large energy deposit per unit length in lower kinetic energies, according to the Bethe formula. For the LaBr₃ scintillators, the energy deposit is a linear function of the incident energy above 3 MeV. Therefore, for electrons above 3 MeV, the incident energy of electrons can be estimated from the energy deposit at LaBr₃. However, we must consider statistical variations in practice. For example, when the energy deposit in LaBr₃ is 2 MeV, the estimated incident electron energy is 3.8–6.7 MeV with one standard deviation, an uncertainty of ~30%. In addition, the energy resolution affects the measurement accuracy of the energy deposits in LaBr₃, which is considered to cause a larger uncertainty. Figure 17 shows only XGRE1, but we obtained the same results for XGRE2 and 3.

Figure 18 shows the effective area of XGRE for electrons. The criteria for electron detection are the same as the analysis above. At an elevation angle of 90 deg, the total effective area of the three sensors is 155 cm² for electrons with an incident energy of 2 MeV, but it monotonically increases with the incident electron energy, and it is 664 cm² for electrons with an incident energy of 10 MeV. The effective areas at an elevation angle of 60 deg were also calculated in the same way as Fig. 16. In the case of electrons, the change in effective area with azimuth angle is observed in the entire energy range of 1 to 10 MeV, and the amount of changes by an incident angle is higher than that of photons.

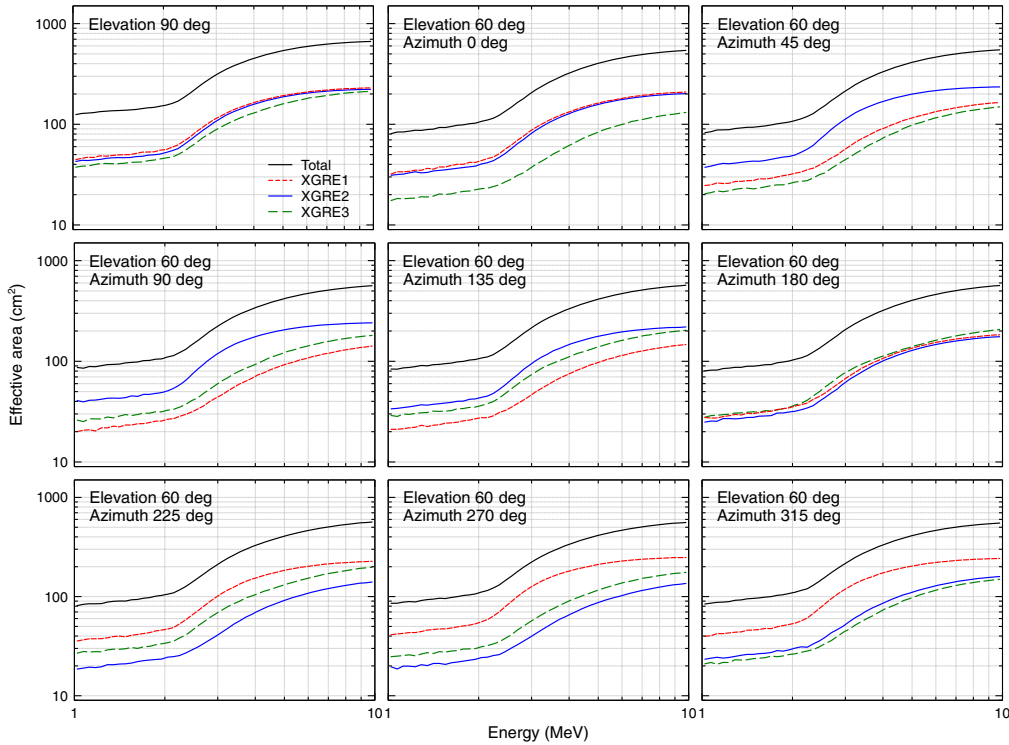


Fig. 18 Effective areas of electrons for various elevation and azimuth angles, as the same condition as Fig. 16.

4.4 Angular Resolution

As shown in Fig. 2, the three sensors of XGRE were mounted at angles, and the effective area changes with elevation and azimuth angles of incident particles on the low-energy side, as shown in Fig. 16. By utilizing this characteristic, the direction of arrival of gamma rays can be measured from the ratio of photon counts of the three sensors. We verified this directional resolution by Monte Carlo simulations. The simulations had the same setup as in Sec. 4.2 [Fig. 12(b)]. Here, the incident particles were gamma rays following the TGF spectrum [Eq. (5)], with a fluence of 3.18×10^3 photons cm^{-2} in 0.04 to 10 MeV. A total of 109 simulations were performed for four elevation angles of 90, 75, 60, and 45 deg and 36 azimuth angles (10-deg interval) for the three elevation angles excluding 90 deg. The thresholds of the LaBr₃ crystals were set to 0.08 MeV for all three sensors.

Figure 19 shows the change in the number of counts of each sensor with respect to the azimuth angle. The number of counts is normalized by the total number of counts of the three sensors at each elevation angle. The count rate of each sensor changes like a sine curve with respect to the azimuth angle. The maximum count values for XGRE1, 2, and 3 at an elevation

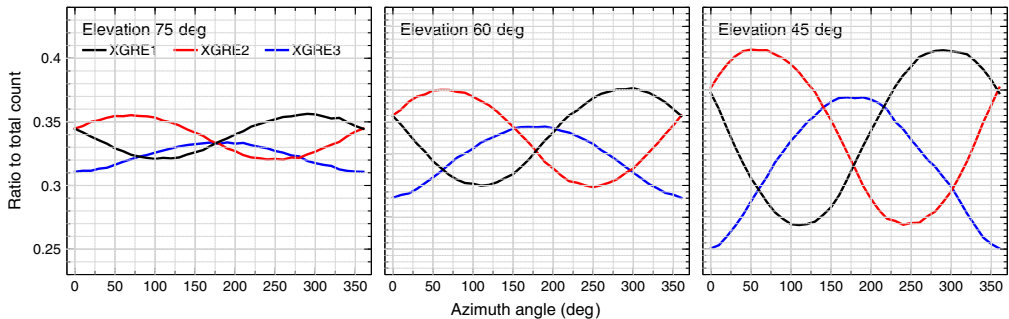


Fig. 19 Relation between azimuth angles of gamma rays and photon counts by XGRE. The photon counts are normalized by the total count of XGRE1–3 at each azimuth angle.

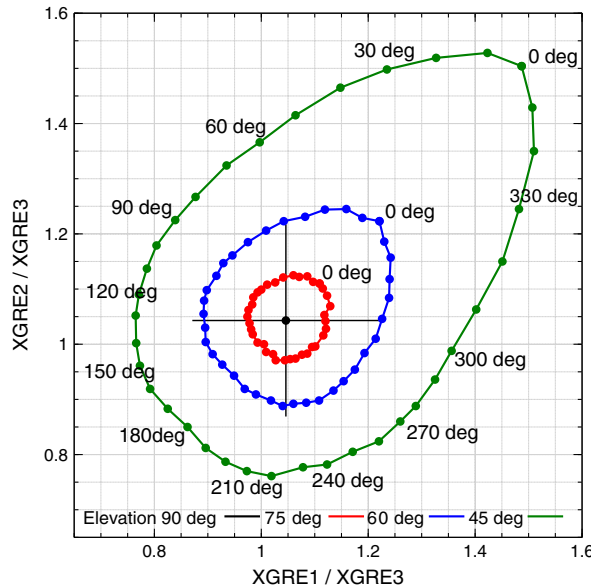


Fig. 20 Relations between the count ratio of XGRE1 to XGRE3 and of XGRE2 to XGRE3 with various elevation and azimuth angles, when assuming a typical TGF photon spectrum (see the main text). The error for the 90-deg-elevation angle indicates a statistical one when considering a typical TGF fluence of 0.65 photons cm⁻². Angles described in the plot are azimuth angles.

angle of 60 deg are at azimuth angles of 300, 60, and 170 deg, respectively. The minimum values are at 110, 250, and 0 deg, respectively. The amount of changes increases as the elevation angle decreases.

A practical method for angle detection is analysis on two-dimensional plots. Figure 20 shows the ratio of the counts of XGRE1 and 2 divided by the count of XGRE3 in the two-dimensional plane. On this plot, the ratio makes an oval orbit as the azimuth changes. The smaller the elevation angle, the larger the oval orbit. Since the orbits are not superimposed, the elevation and azimuth angles can be uniquely determined by two numbers, the count ratio of XGRE1 and XGRE2 to XGRE3, if the count data have enough statistics. On the other hand, in practice, the angle estimation accuracy is limited by statistical errors. The error bar attached to the 90-deg-elevation result shows a statistical uncertainty at one standard deviation when considering the typical TGF fluence of 0.65 photons cm⁻² (0.04–10 MeV). The error bar is superimposed on the orbit of the two-dimensional plane at an elevation angle of 60 deg. Therefore, the azimuth angle cannot be estimated with the typical-fluence TGFs when the elevation angle is 60 deg or above. The estimation accuracy of azimuth angle at an elevation angle of 45 deg is $\sim \pm 30$ deg near azimuth 0 deg, and $\sim \pm 50$ deg near azimuth 180 deg. The estimation accuracy of azimuth angle will be improved for brighter TGFs.

5 Conclusion

XGRE was the key instrument of TARANIS for high-energy atmospheric phenomena such as TGFs and TEBs. It consisted of three sensors with LaBr₃ and plastic scintillators and was sensitive to X-rays, gamma rays, and electrons. The assembly of the flight model started in February 2018, and validation tests of the sensors were performed in Paris, before its delivery to CNES Toulouse in November 2018. XGRE was then mounted on the satellite and experienced environment and calibration tests with the satellite.

Based on the thermal-cycle test performed from April to May 2018, the gain variation by the temperature of XGRE was measured. The correlation between gain and temperature was clear above 20°C but unclear below 20°C. During cold cycles, the energy resolution degraded, and sometimes one emission line from the calibration source was split into two peaks because the two high-voltage modules in one sensor seemed to have slightly different dependence on temperature.

The calibration test with XGRE onboard the satellite was performed from February to March 2020 at CNES Toulouse. The energy range of XGRE for X-ray and gamma rays was determined to be 0.04 to 11.6 MeV, 0.08 to 11.0 MeV, and 0.08 to 11.3 MeV for XGRE1, 2, and 3, respectively. The energy resolution (FWHM) at 0.662 MeV was 20.5%, 25.9%, and 28.6%, respectively.

To investigate the performances of XGRE, a simulation model was developed, and Monte Carlo simulations were performed with Geant4. The model was verified by comparing the result of the calibration test with the satellite, and its uncertainty was less than 15%. The effective area of XGRE, derived from a Monte Carlo simulation with the verified model, reached the maximum at 0.1 MeV, 838 cm², and the minimum at 3.5 MeV, 191 cm², in total for the three sensors. The effective area below 0.3 MeV was sensitive to the elevation and azimuth angle of incident X-rays and gamma rays. Therefore, the arrival angle of photons can be estimated with the ratio of photon counts measured by the three sensors, although the accuracy was limited by the statistical uncertainty of photon counts.

TARANIS was launched on November 17, 2020. However, the mission was lost due to the failure of the launcher. Although XGRE was unable to directly contribute to high-energy atmospheric physics, the knowledge obtained during the development of XGRE will be valuable for a future mission of high-energy atmospheric physics and high-energy astrophysics.

Disclosures

The authors declare no conflicts of interest.

Code and Data Availability

The materials to produce figures in this paper are published and can be obtained on Mendeley Data (<https://doi.org/10.17632/4smf49dyrw.1>). The Geant4 model is available upon request to Y.W. or D.S.

Acknowledgments

TARANIS was the satellite mission led by CNES. The XGRE team is strongly supported by the Centre National de la Recherche Scientifique (CNRS), and CNES. Y.W. is supported by MEXT-KAKENHI of Japan (Grant Nos. 18J13355 and 20K22354), RIKEN Special Postdoctoral Research Program, and the International Joint Research Program of Institute for Space-Earth Environmental Research, Nagoya University.

References

1. V. P. Pasko, Y. Yair, and C.-L. Kuo, “Lightning related transient luminous events at high altitude in the earth’s atmosphere: phenomenology, mechanisms and effects,” *Space Sci. Rev.* **168**(1), 475–516 (2012).
2. J. R. Dwyer, D. M. Smith, and S. A. Cummer, “High-energy atmospheric physics: terrestrial gamma-ray flashes and related phenomena,” *Space Sci. Rev.* **173**, 133–196 (2012).
3. G. J. Fishman et al., “Discovery of intense gamma-ray flashes of atmospheric origin,” *Science* **264**, 1313–1316 (1994).
4. D. M. Smith et al., “Terrestrial gamma-ray flashes observed up to 20 mev,” *Science* **307**(5712), 1085–1088 (2005).
5. S. Foley et al., “Pulse properties of terrestrial gamma-ray flashes detected by the Fermi gamma-ray burst monitor,” *J. Geophys. Res. Space Phys.* **119**, 5931–5942 (2014).
6. M. S. Briggs et al., “First results on terrestrial gamma ray flashes from the Fermi gamma-ray burst monitor,” *J. Geophys. Res. Space Phys.* **115**, A07323 (2010).
7. B. G. Mailyan et al., “The spectroscopy of individual terrestrial gamma-ray flashes: constraining the source properties,” *J. Geophys. Res. Space Phys.* **121**, 11346–11363 (2016).
8. M. Marisaldi et al., “Detection of terrestrial gamma ray flashes up to 40 mev by the agile satellite,” *J. Geophys. Res. Space Phys.* **115**, A00E13 (2010).
9. M. Tavani et al., “Terrestrial gamma-ray flashes as powerful particle accelerators,” *Phys. Rev. Lett.* **106**, 018501 (2011).
10. A. Ursi et al., “Terrestrial gamma-ray flashes in the beppoax data archive,” *J. Atmos. Sol. Terr. Phys.* **156**, 50–56 (2017).
11. T. Neubert et al., “A terrestrial gamma-ray flash and ionospheric ultraviolet emissions powered by lightning,” *Science* **367**, 183–186 (2019).

12. N. Østgaard et al., “First 10 months of TGF observations by ASIM,” *J. Geophys. Res.: Atmos.* **124**, 14024–14036 (2019).
13. A. Gurevich, G. Milikh, and R. Roussel-Dupré, “Runaway electron mechanism of air breakdown and preconditioning during a thunderstorm,” *Phys. Lett. A* **165**, 463–468 (1992).
14. J. R. Dwyer, “Source mechanisms of terrestrial gamma-ray flashes,” *J. Geophys. Res.* **113**, D10103 (2008).
15. B. E. Carlson, N. G. Lehtinen, and U. S. Inan, “Terrestrial gamma ray flash production by active lightning leader channels,” *J. Geophys. Res. Space Phys.* **115**, A10324 (2010).
16. S. Celestin and V. P. Pasko, “Energy and fluxes of thermal runaway electrons produced by exponential growth of streamers during the stepping of lightning leaders and in transient luminous events,” *J. Geophys. Res. Space Phys.* **116**, A03315 (2011).
17. J. R. Dwyer, “A fundamental limit on electric fields in air,” *Geophys. Res. Lett.* **30**, 2055 (2003).
18. J. R. Dwyer, “The relativistic feedback discharge model of terrestrial gamma ray flashes,” *J. Geophys. Res. Space Phys.* **117**, A02308 (2012).
19. J. R. Dwyer, B. W. Grefenstette, and D. M. Smith, “High-energy electron beams launched into space by thunderstorms,” *Geophys. Res. Lett.* **35**(2), L02815 (2008).
20. M. S. Briggs et al., “Electron-positron beams from terrestrial lightning observed with Fermi GBM,” *Geophys. Res. Lett.* **38**, L02808 (2011).
21. D. Sarria et al., “Constraining spectral models of a terrestrial gamma-ray flash from a terrestrial electron beam observation by the atmosphere-space interactions monitor,” *Geophys. Res. Lett.* **48**, e93152 (2021).
22. S. A. Cummer et al., “Lightning leader altitude progression in terrestrial gamma-ray flashes,” *Geophys. Res. Lett.* **42**, 7792–7798 (2015).
23. F. Lyu, S. A. Cummer, and L. McTague, “Insights into high peak current in-cloud lightning events during thunderstorms,” *Geophys. Res. Lett.* **42**, 6836–6843 (2015).
24. F. Lyu and S. A. Cummer, “Energetic radio emissions and possible terrestrial gamma-ray flashes associated with downward propagating negative leaders,” *Geophys. Res. Lett.* **45**, 10764–10771 (2018).
25. Y. Pu et al., “Low frequency radio pulses produced by terrestrial gamma-ray flashes,” *Geophys. Res. Lett.* **46**(12), 6990–6997 (2019).
26. A. Lindanger et al., “Production of terrestrial gamma-ray flashes during the early stages of lightning flashes,” *J. Geophys. Res.: Atmos.* **127**(8), e2021JD036305 (2022).
27. I. Bjørge-Engeland et al., “Terrestrial gamma-ray flashes with accompanying elves detected by ASIM,” *J. Geophys. Res.: Atmos.* **127**(11), e2021JD036368 (2022).
28. F. Lefevre et al., “Taranis—a satellite project dedicated to the physics of TLES and TGFS,” *Space Sci. Rev.* **137**, 301–315 (2008).
29. P. Laurent et al., “On-ground calibrations of XGRE: an ultrafast gamma-ray spectrometer onboard the TARANIS mission for TGF studies,” *Nucl. Instrum. Methods Phys. Res. A* **1047**, 167868 (2023).
30. S. Agostinelli et al., “Geant4—a simulation toolkit,” *Nucl. Instrum. Methods Phys. Res., Sect. A* **506**, 250–303 (2003).
31. J. Allison et al., “Geant4 developments and applications,” *IEEE Trans. Nucl. Sci.* **53**, 270–278 (2006).
32. J. Allison et al., “Recent developments in Geant4,” *Nucl. Instrum. Methods Phys. Res., Sect. A* **835**, 186–225 (2016).
33. C. M. Poole et al., “A CAD interface for GEANT4,” *Australas. Phys. Eng. Sci. Med.* **35**, 329–334 (2012).
34. D. Sarria et al., “TARANIS XGRE and IDEE detection capability of terrestrial gamma-ray flashes and associated electron beams,” *Geosci. Instrum. Methods Data Syst.* **6**, 239–256 (2017).

Yuuki Wada is an assistant professor at the Graduate School of Engineering, Osaka University. He received his PhD in physics from the University of Tokyo in 2020. He was a visiting researcher at the Astroparticle and Cosmology (APC) laboratory in Paris, France, in 2018 and 2020, working for on-ground calibration campaigns of the TARANIS/XGRE. His current research interests include high-energy atmospheric physics, meteorology, radar remote sensing, and radiation measurements.

Philippe Laurent is employed at the CEA Astrophysical Department in Saclay and Astroparticle and Cosmology (APC) laboratory in Paris, France. He specializes in high-energy astrophysics and got his PhD in 1992, studying high-energy emission from black holes X-ray binaries. He has been participating in the ESA/INTEGRAL gamma-ray mission since 1995 and is now the INTEGRAL/IBIS telescope Co-PI. He was also a PI of the TARANIS/XGRE instrument developed at the APC laboratory.

Ion Cojocari was an instrumentation engineer at the Astroparticle and Cosmology (APC) laboratory, having participated in the integration, testing, and calibration of the XGRE instrument. He obtained his PhD in physics, developing Compton polarimeters dedicated to measuring

gamma-ray polarization. He is currently employed at IJCLab, developing low-threshold cryogenic germanium detectors to be used in the next generation of low-mass dark matter search experiments.

Stéphane Colonges is an expert in reliability engineering at the APC laboratory of CNRS. He was involved in the TARANIS mission as a product assurance engineer.

David Sarria is a researcher at the Birkeland Centre for Space Science, the University of Bergen in Norway. He received his PhD from the Institut de recherche en astrophysique et planétologie at the University of Toulouse in 2015 and is a post-doctoral researcher at the Astroparticle and Cosmology (APC) laboratory at the University of Paris Diderot on the TARANIS spacecraft, particularly on Monte-Carlo modeling of the XGRE instrument.

Kazuhiro Nakazawa is an associate professor at Nagoya University, focusing on X-ray and MeV gamma-ray astronomy in both observational and detector development aspects, including on-ground thundercloud gamma-ray observations. He received his PhD from the University of Tokyo in 2001. He has long experience in in-orbit crystal scintillator detector development.

Biographies of the other authors are not available.